Construction and Building Materials 403 (2023) 133062

Contents lists available at ScienceDirect

Construction and Building Materials

journal homepage: www.elsevier.com/locate/conbuildmat

Time–frequency analysis of ultrasonic signals for quality assessment of bonded concrete

Pooria Khademi [a], Mohsen Mousavi [b,c], Ulrike Dackermann [b], Amir H. Gandomi [c,d,*]

[a] Department of Civil Engineering, Sharif University of Technology, Tehran, Iran
[b] School of Civil and Environmental Engineering, The University of New South Wales, Sydney 2052, Australia
[c] Faculty of Engineering and IT, University of Technology Sydney, Ultimo, NSW 2007, Australia
[d] University Research and Innovation Center (EKIK), Óbuda University, 1034 Budapest, Hungary

ARTICLE INFO

Keywords:
Bi-surface shear test
Ultrasound test
Variational mode decomposition
Machine learning

ABSTRACT

In accelerated bridge construction (ABC), 3D-printed concrete and structural retrofitting using concrete jacketing are used to reduce the onsite construction time. Both techniques involve bonded concrete, where a concrete layer is cast on the old substrate. As a result, the interfacial transition zone between these concrete layers is the weakest part of the structure. In this paper, a machine learning-based model is proposed to predict the bond strength between concrete layers from extracted ultrasonic features. Ultrasound tests provide the input parameters, and bi-surface shear test results are the targets for the machine learning model. To validate the method, laboratory testing is performed on 54 concrete specimens with different design mixtures and bond zone conditions. Variational Mode Decomposition (VMD) is applied to the ultrasonic signals, and three intrinsic mode functions (IMFs) are extracted from each signal leading to 21 independent features. Four machine learning algorithms are deployed, namely K-nearest-neighbors, support vector machine, random forest, and XGB regressors. XGB is found to be the most accurate model, and its hyperparameters are tuned to optimize the model performance. To improve the method, the features' importance values are derived, and the most compelling features for training are identified, which are the third quartile and center frequency of the first IMF's instantaneous frequency, and the center frequency and kurtosis of the second IMF's instantaneous frequency. The resulting final model was a tuned XGBoost regression model that obtained an R-squared value of 95.5 percent taking the four features as input. For the four selected features, apparent clustering was found at a bond strength of 3 MPa, ensuring a reliable prediction of quality bond conditions. These results demonstrate the effectiveness of the proposed model in predicting the bi-surface shear strength of concrete layers based on ultrasonic testing.

1. Introduction

Many civil applications require a concrete overlay to be retrofitted to an existing layer of concrete. In accelerated bridge construction (ABC), concrete is added layer-by-layer in 3D printing, and different concrete layers are bonded in the connection of prefabricated bridge decks. A challenge for these construction methods is the bonding strength of the interfacial transition zone between concrete layers. High-performance concrete (HPC) is suitable for 3D printing, rehabilitation, and fast construction due to its high strength and flowability. Since HPC shows higher bonding to the substrate than ordinary concrete, it is preferable for rehabilitation. The condition of the substrate's surface plays an important role in the bonding strength, and surface treatments can be applied to improve the bond strength by increasing the friction and adhesion between the layers. Surface treatment methods include wire brushing the substrate [1,2], using steel connections between the layers, and adding grooves on the substrate surface [3]. Further, the moisture at the interfacial transition zone can affect the bond quality adhesion adversely [4]. Hence, to determine the actual bonding strength, it is essential to conduct destructive or non-destructive tests due to the multiplicity of influencing parameters, such as surface treatments and material.

Many destructive test setups have been proposed to evaluate the bond strength between concrete layers: including slant shear, splitting prism, pull-off, and bi-surface shear. Zanotti et al. [5] compared tensile and shear bond strength tests, and found that shear tests are more

* Corresponding author at: Faculty of Engineering and IT, University of Technology Sydney, Ultimo, NSW 2007, Australia.
E-mail addresses: pooria.khademi04@icloud.com (P. Khademi), mohsen.mousavi@unsw.edu.au (M. Mousavi), u.dackermann@unsw.edu.au (U. Dackermann), gandomi@uts.edu.au (A.H. Gandomi).

https://doi.org/10.1016/j.conbuildmat.2023.133062
Received 16 March 2023; Received in revised form 16 August 2023; Accepted 18 August 2023
Available online 31 August 2023

reliable since tensile tests produced scatter results. Momayez et al. [6] investigated the test accuracy and performance of various bond strength tests and recommended the bi-surface shear test due to its acceptable coefficient of variation (COV) and ease of use.

Due to the degradation of bond strength, it is vital to regularly assess the bonding condition during the service life of a structure to ensure sufficient concrete bonding. Ultrasound testing (UT) is a Non-Destructive Evaluation (NDE) method that is suitable for initial strength estimation, internal defect detection [7], and structural health monitoring (SHM). There are two types of ultrasonic test setups: non-contact and contact. Non-contact ultrasound testing has some limitations, such as being expensive and sometimes only applicable in conductive mediums (as for the electromagnetic induction of ultrasonic waves). Therefore, contact ultrasound testing is more common in concrete materials due to their relatively low price and ease of use. Conventional ultrasonic testing is mainly based on the correlation between the wave velocity passing through the medium and the compressive strength of the concrete [8,9]. However, other features considering the shape of the transmitted wave and the wave energy can produce more precise strength estimations and are more indicative in damage detection than the wave velocity [10–15].

Guided wave ultrasonic testing (GWUT) involves the study of more complex underlying physics by considering the wave's shape. In GWUT, a signal with a predetermined wave shape is emitted and the returning shape is recorded after passing through the medium. Many features can be extracted from GWUT, such as the energy, amplitude, and attenuation of the wave, or the deformation of the mode shape. However, some factors may affect the testing results, such as the amount of grease as couplant [16–18] used to connect the transducer/receiver to the specimen surface, and the applied pressure to the transducer/receiver by the user. Due to these challenges, techniques are being developed that can generate accurate results regardless of the influencing factors.

Huang et al. [19] proposed the empirical mode decomposition (EMD) method as a self-adaptive signal processing technique that is advantageous in the analysis of non-stationary signals. This method can be used to decompose bulk waves into an empirical number of intrinsic mode functions (IMFs), reflecting the input signals' intrinsic information. EMD has many advantages over other time–frequency signal decomposition algorithms, such as Wavelet Transform (WT). For instance, it can pass nonlinear modulations in the original signal to the decompositions. Moreover, the major advantage of EMD is that mother wavelet functions are derived from the signal itself. Hence, this adaptive analysis differs from wavelet-based approaches with fixed mother wavelet functions. However, EMD has disadvantages such as mode mixing, separated spectral bands, and a random number of modes generation which is not under the user's control [20]. Control over the number of extracted modes is crucial for training a machine learning (ML) algorithm since the number of inputs depends on the number of extracted modes from the signals.

Variational mode decomposition (VMD) is a nonlinear/nonstationary signal decomposition algorithm proposed by Dragomiretskiy and Zosso [21] to improve the disadvantages of EMD. VMD yields better results than EMD in terms of frequency recovery [22], and it is an entirely non-recursive method that can be used to decompose bulk waves into IMFs, where the modes are extracted concurrently. Each IMF has its center frequency, and the sum of all IMFs can reproduce the original input signal minus some noise, depending on settings. After demodulating the original signal, the resulting IMFs have a narrow frequency bandwidth and are smooth. Since the user of VMD can select the number of decompositions based on the problem circumstances, most of the time, it provides fewer decompositions than EMD [23]. Therefore, mode mixing in the VMD method is less likely to occur than in EMD. The number of modes is optional (adaptive bands) in VMD, and there is an important relation to Wiener filter denoising. Determining the number of modes by the user allows for extracting adequate IMFs to be used as input features in artificial intelligence algorithms.

The use of Artificial Intelligence (AI) has become increasingly popular in civil engineering applications. Machine learning (ML), deep learning (DP), and fuzzy logic (FL) have been deployed to solve various correlation problems performing actions such as interpreting, clustering and classification, reasoning, learning, and decision-making [24–26]. Popular ML algorithms used by academics and the industry are scalable tree-boosting systems called XGBoost (XGB) [13,27,28]. The scalability of XGB is due to a novel tree learning algorithm for handling sparse data and a theoretically justified weighted quantile sketch procedure for handling instance weights in approximate tree learning. In concrete technology, XGB has been used to estimate the compressive strength of concrete and showed acceptable accuracy [29]. Besides XGB, there are other algorithms such as random forest (RF), support vector machine (SVM), and K nearest neighbor (KNN). Mousavi et al. [13] investigated the capabilities of KNN and SVM for wood classification and achieved high accuracies.

Although several studies have presented methods analyzing results from tests, such as slant shear, splitting prism, pull-off, and bi-surface shear, to evaluate the bonding strength between concrete blocks, none have explicitly developed a machine learning model to predict this quality using features extracted from nondestructive testing (NDT) techniques. This paper addresses this shortcoming developing a technique that leverages ultrasound testing, advanced signal processing, and machine learning to create a model capable of non-destructively estimating the bonding strength between concrete blocks.

This paper proposes a systematic feature extraction approach analyzing ultrasonic bulk waves for ML training to predict the bi-surface shear strength of concrete layers. In this regard, non-destructive and destructive tests were conducted on the same samples to measure ultrasonic wave signals and to determine the corresponding bond strengths. The captured wave signals were decomposed using VMD, and features were extracted from the sub-signals. Machine learning algorithms were trained to predict the specimens' bond strength using the extracted features. As such, the input parameters to the regression models are the features extracted from the ultrasonic waves, and the target is the bond strength obtained from destructive bi-surface shear testing. An optimization study was performed to select the most effective features, and different machine learning models were deployed to produce the best model predicting the bi-surface shear strength.

2. Problem statement and objectives

In accelerated bridge construction (ABC), structural retrofitting, and 3D concrete printing, it is vital to assess the bonding quality between different layers of concrete to ensure structural integrity. Failure of bonded concrete typically starts from the weakest part of these structures, i.e., their bonding zone. Hence, the condition of this critical interfacial transition zone needs to be evaluated throughout their service lives. Ultrasonic testing is one of the most effective non-destructive testing (NDT) procedures and can be used for this purpose. However, only limited work has been conducted on using UT for concrete bond strength assessment.

This research aims to provide a high-accuracy model for unsupervised health monitoring of the bonding zone in bonded concrete structures from non-destructive ultrasonic signals. To this end, VMD is applied to the ultrasound signals, and the performance of four machine-learning algorithms is studied. To achieve the most effective and high-accuracy model for bonding strength prediction, the proposed method applies wave feature optimization procedures leading to significantly reduced wave features and highly accurate assessment results. The research is supported by the laboratory testing of 54 concrete specimens with various bond zone conditions and concrete mixtures, and 162 ultrasound tests (three tests for each specimen) are conducted. To establish the ground truth of the bonding strength, destructive bi-surface shear testing is performed on all tested specimens.

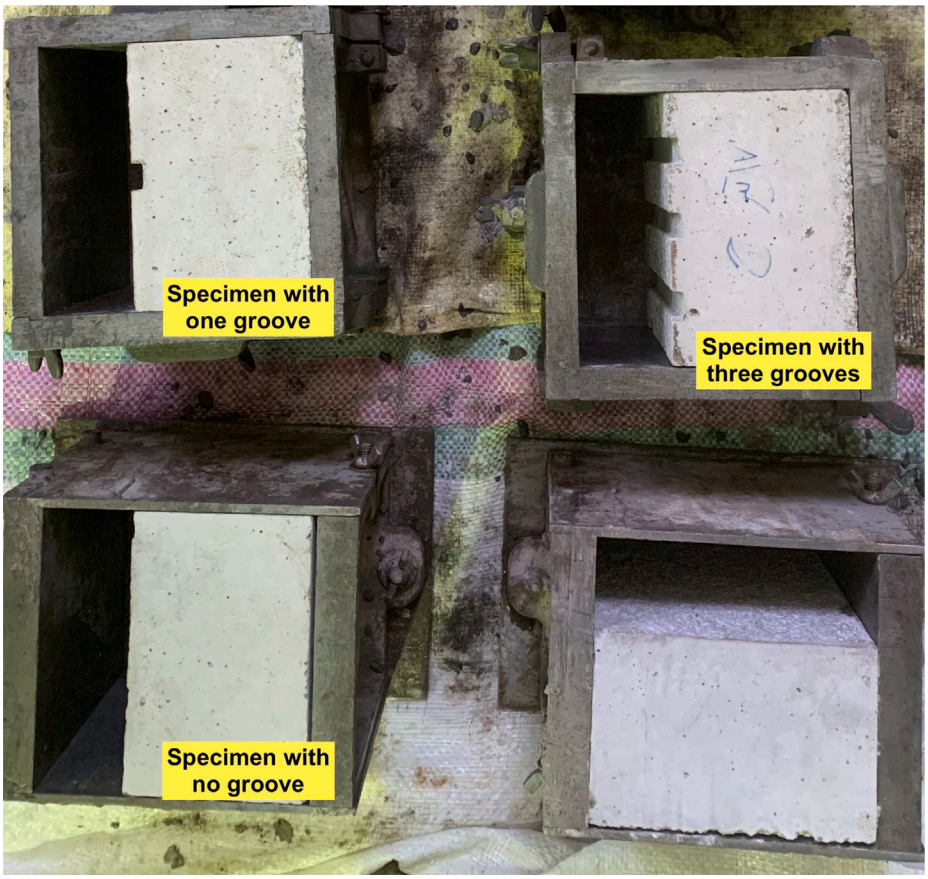

Fig. 1. Specimens with different surface treatment.

3. Materials and sample preparation

For laboratory testing, high-performance alkali-activated slag concrete (HPAASC) was used as overlay material on ordinary Portland cement concrete (OPCC). Using slag as a substitution for Portland cement is common for research in this field [30,31]. The HPAASC mixture consisted of sand, ground granulated blast furnace slag (GGBFS), silica fume, a mixture of sodium hydroxide and sodium silicate solution, a superplasticizer, and steel fiber. The substitution of GGBFS for cement makes this concrete eco-friendly since GGBFS is a waste material from iron production. The mixed sodium hydroxide and sodium silicate solution work as an activator in the slag hardening process. The sand content and superplasticizer amount were fixed at 1000 kg/m^3 and 27 kg/m^3 in all the samples. On the other hand, the silica fume, steel fiber, GGBFS, activator solution, and surface roughness varied among the samples. Table 1 lists the deployed range of various concrete design parameters. The maximum and minimum values are based on typical practical usage. For instance, we applied a maximum of 12 moles of sodium hydroxide solution since for high-performance concrete the molarity of the sodium hydroxide reduces the flowability [3].

The different concrete mixtures were cast on 10 × 15 × 15 cm^3 blocks of OPCC in a 15 × 15 × 15 cm^3 mold. Therefore, cubic samples with a dimension of 15 cm at each side, one-third made of HPAASC and two-thirds made of OPCC, were obtained. The contact surface between OPCC and HPAASC was investigated for three conditions: untreated, one-line groove, and three-line groove (see Fig. 1). Hence, the surface roughness of the bond zone differed across the studied specimens.

Table 1
The range of the mixed designs parameters.

Variable	Minimum	Maximum
Slag (kg)	704	836
Silica Fume (kg)	44	176
Steel Fiber (Percent)	0	2
The Molarity of NaOH (mol)	8	12

4. Test setup

Two different types of tests were carried out: non-destructive and destructive. One month after sample preparation, ultrasound testing was performed on the specimens to capture non-destructive ultrasonic wave signals containing information on the samples' material properties. Thereafter, destructive bi-surface shear testing was conducted to measure their bonding strength (in MPa). The raw ultrasonic signals were subsequently used as inputs to the ML model, and the measured bond strengths as the model's targets. Fig. 2 shows a schematic overview of the research methodology. Comprehensive details on these tests are provided in the subsections below.

4.1. Destructive test

In this research, bi-surface shear testing was conducted due to its acceptable coefficient of variation compared to other test methods. A schematic of the testing is depicted in Fig. 3(a). As can be seen, the tested sample was placed on two supports positioned at the bottom corner sides of the specimen, and a load was applied to a third support positioned at the top center. The three supports had a width of 5 cm and a length of 15 cm. A universal testing machine was employed to apply the load with a maximum capacity of 1000 kN on the top support. Thereby, the top support provides two shear planes passing through the OPCC substrate and the bond zone. Since one-third of a test specimen is made of HPAASC, and two-thirds made of OPCC, the failure may occur either in the OPCC or the bond zone. As a result, substrate failure

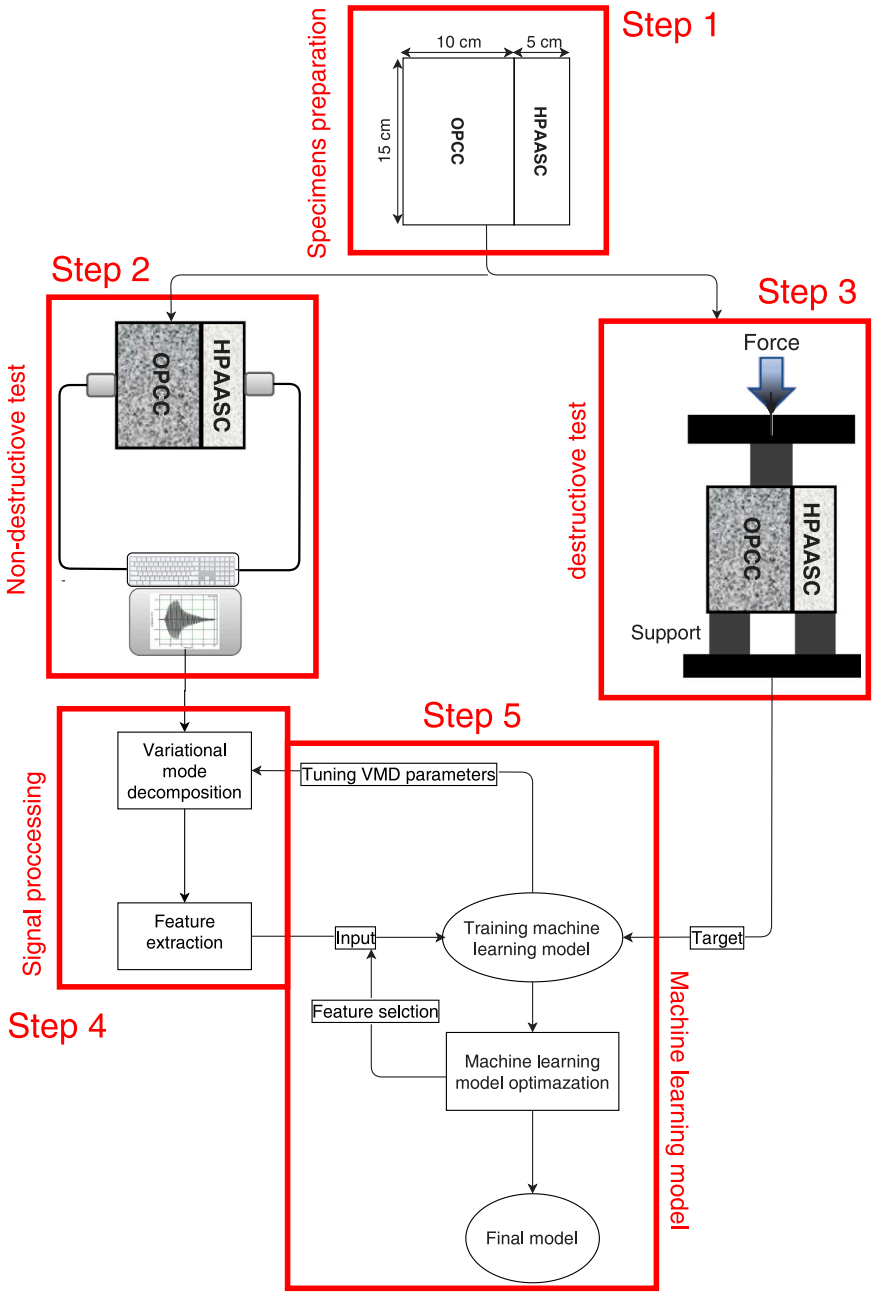

Fig. 2. The graphical abstract.

occurs when the bond strength is higher than the shear strength of the substrate. Fig. 3(b) shows the failure of a test specimen at the bond zone. In the specimens with grooves, the direction of the grooves was perpendicular to the loading direction. Eq. (1) shows an expression for calculating shear strength experimentally.

$$\tau = \frac{P}{2bd} \tag{1}$$

where τ is the bi-surface shear stress, P is the applied load, and b and d are the width and height of the tested specimen, respectively.

OPCC, which had the same mix design in all samples, had a compressive strength of 38 MPa after 28 days. For HPAASC, the design mixtures varied from sample to sample and the compressive strength after 28 days was between 94 and 127 MPa.

4.2. Non-destructive test

In civil engineering structures, non-destructive testing is typically performed to detect damage or to determine material properties. As such, ultrasonic waves can be used to predict the strength of concrete. In this research, ultrasonic testing (UT) is used to assess the bond strength between different layers of concrete. In the UT process, a piezoelectric transducer sends an initial wave, and after the wave passes through the specimen medium, another piezoelectric sensor (receiver) receives the signal. Two main issues can affect the UT test results. First, the amount and type of the couplant material used as a coupling to bridge the gap between the transducer/receiver and the specimen's rough surface allowing transmission of the ultrasonic wave. Therefore, in this study, all specimens were tested with the same type and amount

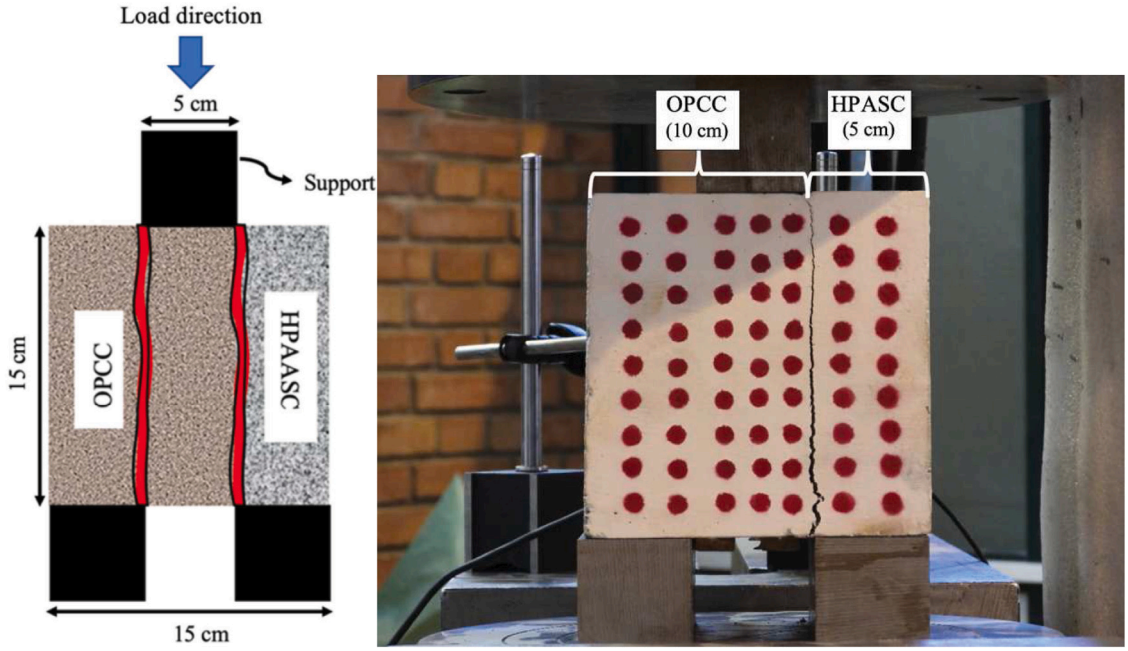

Fig. 3. BSS test configuration.

of couplant. And second, the pressure applied to the transducer and receiver should be the same for all tests to obtain a consistent connection to the specimen's surface. To this end, the transducer/receiver was fixed to the specimen's surface by elastic ribbons of the same length. While aiming to execute standardized testing, in practice, small variations are unavoidable.

The test setup consisted of a function generator (MEGATEK, MFG-2205P), a broadband longitudinal piezoelectric transducer with a center frequency of 100 kHz, a receiver, an amplifier, and a digital oscilloscope (OWON, TDS-7104) to record the longitudinal wave response. In the testing, the function generator produces the waveform, and the digital oscilloscope displays the received amplitudes and waveform. The received signal is weaker than the transmitted signal due to wave transmission effects in the heterogeneous concrete material as well as in the bond zone, such as wave attenuation, dispersion, reflection, and refraction effects. While the initial wave is a longitudinal wave with a sinusoidal pattern, the received signal is a modulated form of the initial wave.

As mentioned previously, three types of surface treatment were studied: without grooves, one groove, and three grooves. Fig. 4 shows the raw signals of three samples with different surface treatments but the same concrete mixtures. The aggregates' different amounts, sizes, and locations have an influence on wave transmission, and hence, waveform detection [32]. Therefore, samples with the same concrete design were selected to minimize the effect of the aggregates. As can be seen in Fig. 4, the different bond conditions resulted in different received waveforms. The highest amplitude is related to the specimen with three grooves due to the higher consistency between concrete layers.

One of the aims of this article is to construct a model that enables the prediction of the bonding strength of concrete overlay using imperfect ultrasound test results. It is a common practice in data science to assess the performance of a machine learning model when imperfect data is available. Moreover, sometimes we intentionally contaminate the data with various types of noise and uncertainties for two primary reasons: (1) data augmentation, and (2) assessing the power of a machine learning model. For example, in the newly added Refs. [33–35] the authors introduce several uncertainties to the training and test ultrasound signals, such as noise contamination and down-sampling, to assess the performance of the proposed machine learning algorithm. As such, we argue that the primary objective of this paper is not to rely on perfectly acquired data. On the contrary, the aim is to develop a machine-learning model that regardless of the quality of the recorded ultrasonic signals, can make satisfactory predictions.

4.3. Features extraction

To relate the specimen's physical strength to the ultrasound measurements, the measured ultrasonic signals must be interpreted. Variational mode decomposition (VMD) is an effective signal processing tool that can be used to decompose an input signal into different band-limited IMFs. VMD aims to decompose the input signal into a prespecified number of discrete and narrow-band sub-signals along with their center frequencies. It is an adaptive signal decomposition algorithm that can adapt to the original signal characteristics while the sum of the sub-signals constructs the original signal minus some noise depending on settings. Fig. 5 showcases an example of an ultrasound signal that passed through a specimen and then divided into three IMFs using VMD. Fig. 5(a) shows a received signal used as an input of VMD, which is further decomposed into three sub-signals as shown in Figs. 5(b) to 5(d). The first mode (Fig. 5(b)) inherits most of the characteristics of the raw signal (Fig. 5(a)). On the other hand, the second and third modes contain supplementary information representing high-frequency modulations due to the wave interaction with concrete aggregates. In this study, VMD was preferred over other decomposition algorithms due to the following reasons:

1. VMD is capable of computing the center frequency of a signal while maintaining narrow-band properties aligning with the current standard IMF definition.
2. Unlike EMD, VMD decomposes the input signal into a prespecified number of IMFs, making it easy to set up the feature space for the regression problem of this paper.
3. VMD is also capable of noise cancellation, so in severe cases, the noise cancellation property of VMD can be adjusted by tuning the corresponding parameter.

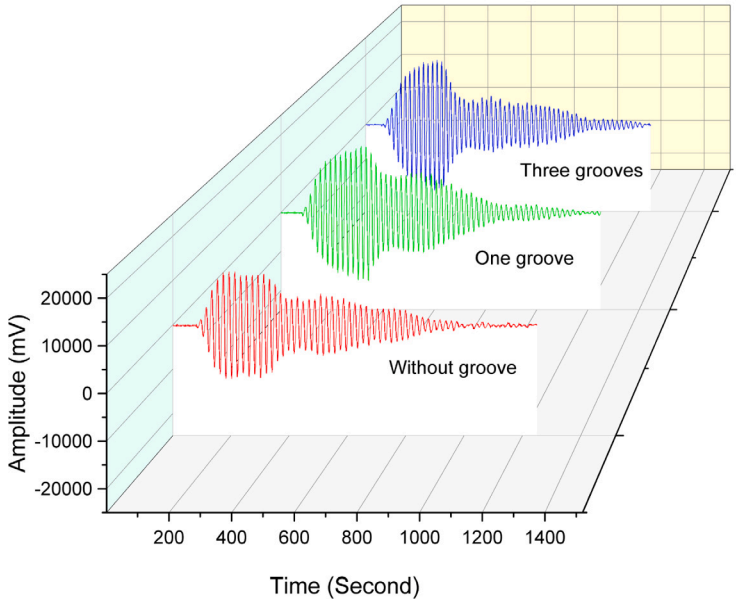

Fig. 4. Waveforms of samples with different surface treatments.

Intrinsic Mode Functions are defined as amplitude-modulated-frequency-modulated (AM-FM) signals. Eq. (2) shows the general form of an IMF considered by VMD:

$$u_k(t) = A_k(t)\cos(\phi_k(t)), \tag{2}$$

where $u(t)$ is the kth IMF, $A_k(t)$ is its instantaneous amplitude which is a non-decreasing function, and $\alpha_k(t)$ is its instantaneous phase.

The 1-D Hilbert transform is the linear, shift-invariant operator that maps all 1-D cosine functions into their corresponding sine functions. It is an all-pass filter that is characterized by the following transfer function:

$$h(\omega) = -j\ \mathrm{sgn}(\omega) = \frac{-j\omega}{|\omega|} \tag{3}$$

Thus, the Hilbert transform is a multiplier operator in the spectral domain. The corresponding impulse response is $h(t)$. Because convolution with $h(t)$ is not integrable, the Hilbert transform of a signal is the convolution integral as below:

$$\hat{h}(t) = \lim_{\epsilon\to 0}\frac{1}{\pi}\int_{|\tau-t|>\epsilon}\frac{g(\tau)}{t-\tau}\,d\tau, \tag{4}$$

where $\hat{h}(t)$ indicates the Hilbert transform of the signal $h(t)$ in which the limit conforms to the Cauchy principal value [36]. The integral of Eq. (4) is convergent, and thus the Hilbert transform of (4) exists.

Before applying VMD to a signal, its parameters need to be specified based on the algorithm developed by the authors of VMD, as presented in [37]. The function of each parameter and the way of specifying them are fully discussed in [12,13]. The values assigned to the VMD parameters in this study are shown in Table 2. As one of the VMD advantages over EMD, p is an integer – the number of IMFs – that the user can determine based on their extensive domain knowledge.

In this research, after selecting different values for p, it was noted that redundant IMFs were extracted from the ultrasonic signals for more than three decompositions. When p was set to a value smaller than three, only a little information about high-frequency modulation could be extracted from the signals.

By further analyzing the IMFs, useful features were extracted from each sub-signal. Each mode has an instantaneous frequency $\left(\frac{d\phi(t)}{dt}\right)$ which is non-decreasing, varies slowly, and is concentrated around a central value f_c. The center frequency (f_c) of a mode is computed by

Table 2
VMD parameters.

Parameters	Description	Specified values
p	Number of IMFs	3
α	Denoising factor	1
τ	Time interval	0.1
ϵ	Convergence threshold	10^{-6}
init	Center frequency initializer	0
DC	Boolean parameter	0

(5) through iterations:

$${f_c}_k^{n+k} = \frac{\int_0^\infty |U_k^{n+k}(f)|^2 f\,df}{\int_0^\infty |U_k^{n+k}(f)|^2\,df} \approx \frac{\sum f|U_k^{n+k}(f)|^2}{\sum |U_k^{n+k}(f)|^2\,df}, \tag{5}$$

where f_c is the kth center frequency, $U_k^{n+k}(f)$ is the Fourier transform of the kth mode calculated in the $(n+1)$th iteration. The kurtosis, variance, and skewness of an IMF's instantaneous frequency were calculated and taken as features through (6), (7), and (8), respectively:

$$K = \frac{\mu_4}{\sigma^4}, \tag{6}$$

where μ_4 is the fourth central moment, and sigma is the standard deviation.

$$S^2 = \frac{\sum (y_i\text{-}\hat{y})^2}{\sum n-1}, \tag{7}$$

where y_i is the value of the ith observation, $\hat{y}$ is the mean value of all observations, and n is the number of observations.

$$\tilde{\mu}_3 = \frac{\sum_i^N (y_i\text{-}\hat{y})^3}{(N-1)\sigma^3}, \tag{8}$$

where N is the number of variables in the distribution. In addition, the first, second, and third quartiles of each IMF's instantaneous frequency were also taken as features. As a result, seven features were obtained from each IMF.

As mentioned above, our preliminary studies showed that decomposing the bulk signal into less than three sub-signals results in missing information about nonlinear modulations in the signal. On the other hand, more than three sub-signals generated redundant information. Therefore, the optimal number of IMFs for this study was chosen as three. This is compatible with the results in [12,13]. Hence, overall, 21

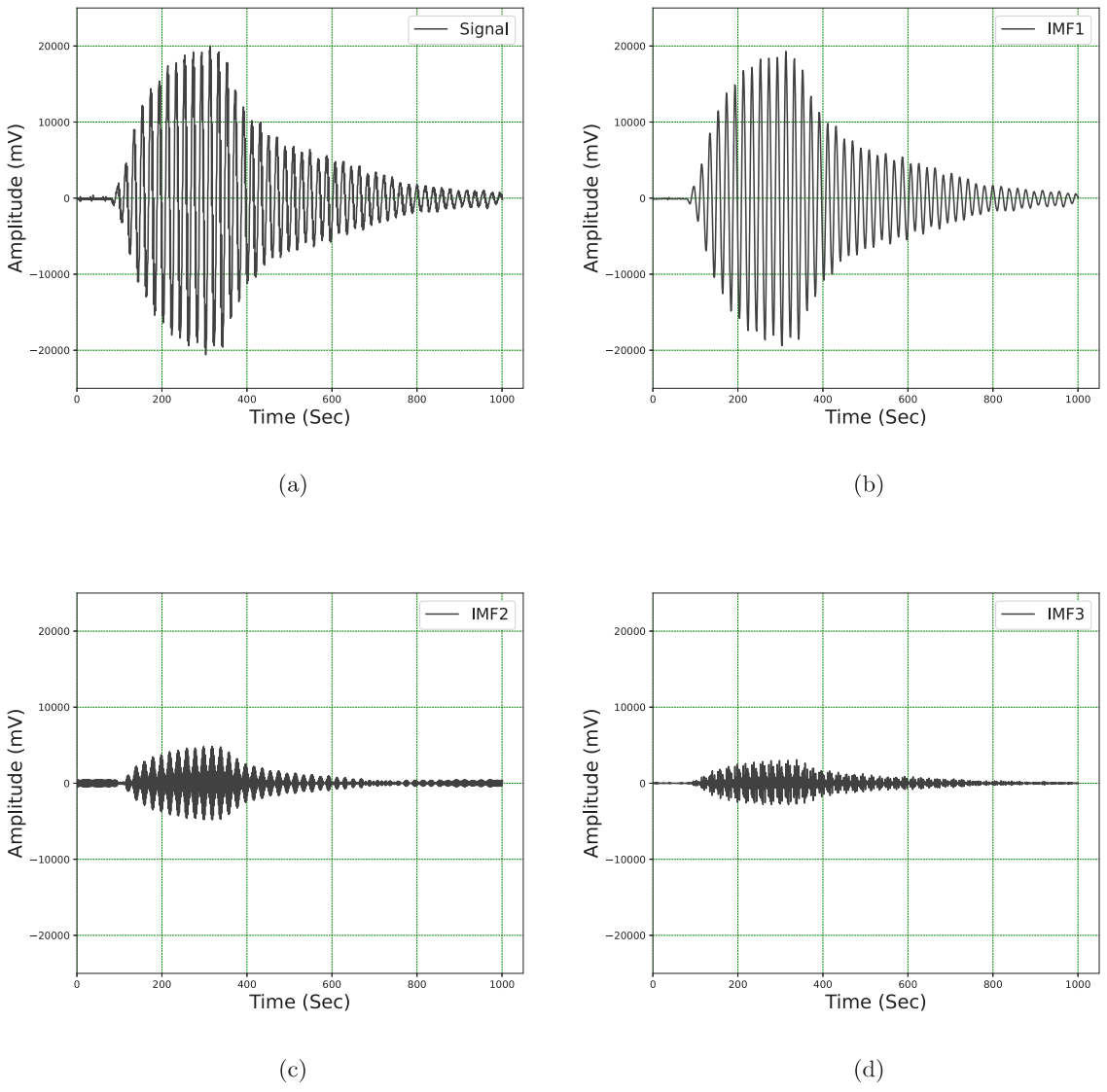

Fig. 5. a: Input signal, b: First mode, c: Second mode, d: Third mode.

independent features (3 IMFs x 7 features) were extracted from each original bulk ultrasound. To investigate whether all these features are essential, and to optimize the algorithm, we applied feature engineering to find the optimal number of features.

5. Machine learning results

Machine learning algorithms were employed to establish a correlation between the extracted features and the mechanical bond strength of the tested specimens. 54 signals resulting from the test samples were investigated. From each signal, 21 features were extracted and used as input vector for four machine learning models, i.e. RF, KNN, SVM, and XGB models. The deployed algorithms were subsequently evaluated to find the best-fitted model.

The box and Whisker plot of Fig. 6 shows the distribution of the extracted features. These features are the inputs of the machine learning algorithms, and the bi-surface shear strength is the output. The samples are made of ordinary Portland cement concrete (OPCC) as the substrate and high-performance alkali-activated slag concrete (HPAASC) as the overlay layers. The OPCC had the same mix design in all samples, and its compressive strength after 28 days was 38 MPa. It is worth noting that the design mixture of HPAASC varies from sample to sample. As such, the compressive strength of the HPAASC concrete after 28 days was between 94 and 127 MPa.

Comparing the accuracy of the trained models showed that XGB achieves the best performance among all models. XGB is based on gradient-boosting on parallel trees and combining the results [38]. XGB is easier to use for tabular structured data as opposed to deep learning, which performs better on non-structured data such as images. Eq. (9) shows the objective function of XGB for finding the function f_t to be fitted on data at the tth iteration of running the algorithm:

$$R^{(t)} = \sum_{i=1}^{n} r\left(y_i, \hat{y}_i^{(t-1)} + f_t(x_i)\right) + \omega(f_t), \tag{9}$$

where r is the XGB's loss function, y_i and $\hat{y}_i$ are real and predicted values, and ω is a penalty factor calculated from Eq. (10) as follows:

$$\omega(f_k) = \gamma T + \frac{1}{2}\lambda\|w\|^2, \tag{10}$$

Variables of XGB include learning rate, max depth, and the number of estimators. Each parameter affects the accuracy of the XGB regressor. Therefore, they need to be tuned to optimize the model's performance. Table 4 shows the variables range used in iterations. A small learning rate may result in finding a local extremum of the graph, whereas the global extremum may not be found by choosing a big learning rate.

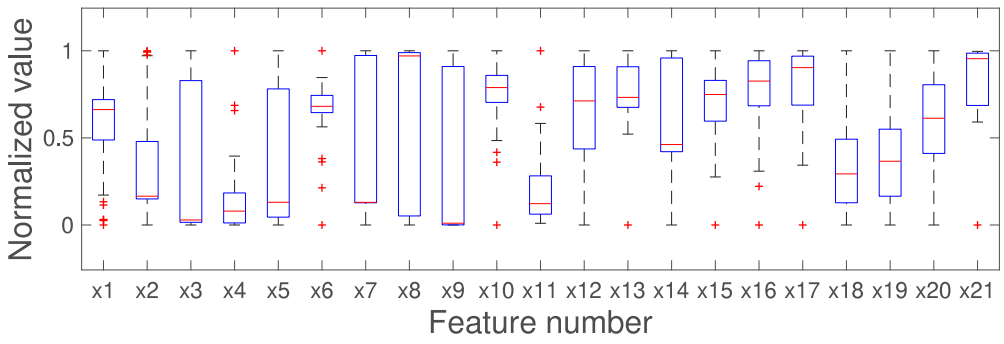

Fig. 6. Box and Whisker plot of the normalized features.

Table 3
Time–frequency features extracted from the ultrasonic test results.

Feature number	Designation	Feature number	Designation
x_1	First quartile of IF_{IMF1}	x_{12}	Kurtosis of IF_{IMF2}
x_2	Second quartile of IF_{IMF1}	x_{13}	Skewness of IF_{IMF2}
x_3	Third quartile of IF_{IMF1}	x_{14}	Center frequency of IMF2
x_4	Variance of IF_{IMF1}	x_{15}	First quartile of IF_{IMF3}
x_5	Kurtosis of IF_{IMF1}	x_{16}	Second quartile of IF_{IMF3}
x_6	Skewness of IF_{IMF1}	x_{17}	Third quartile of IF_{IMF3}
x_7	Center frequency of IMF1	x_{18}	Variance of IF_{IMF3}
x_8	First quartile of IF_{IMF2}	x_{19}	Kurtosis of IF_{IMF3}
x_9	Second quartile of IF_{IMF2}	x_{20}	Skewness of IF_{IMF3}
x_{10}	Third quartile of IF_{IMF2}	x_{21}	Center frequency of IMF3
x_{11}	Variance of IF_{IMF2}	–	–

Table 4
XGB optimization.

Variable	Minimum	Maximum	Optimal value
Learning rate	0.01	0.2	0.1
Max depth	1	15	3
Number of estimator	10	1000	100

Wrong max depth and the number of estimators can either decrease the accuracy of the models or cause over-fitting. Therefore, tuning these hyperparameters enhances the model accuracy [39]. The optimized value for the learning rate, max depth, and the number of estimators was evaluated as 0.1, 3, and 100, respectively.

Table 5 shows the R-squared of each model. The R-squared was computed as follows:

$$\text{R-squared} = 1 - \frac{SS}{TS} \tag{11}$$

where SS is the sum of squares of residuals and TS is the total sum of squares.

The dataset was shuffled and split into four control volumes (CV), and the accuracy pertaining to each CV was reported. The accuracy of XGB was higher than other algorithms, so we chose to tune the XGB models' hyperparameters. After the tuning process, the highest accuracy among the models belonged to the optimized XGB (see Table 6). Fig. 7 shows the loss functions of each fold to monitor the possibility of overfitting. They show a continuous decrease in the loss value of the validation data and no divergence between train and validation data is detected. Therefore, the optimized XGB model was selected for the feature engineering process in the next section. In addition, Fig. 8 shows the accuracy of the model with respect to the training data volume which proves that the training dataset was adequate due to the adequate increase in test data accuracy.

5.1. Feature engineering

From the extracted 21 features, several selected features are directly correlated with accuracy, and ease of use and have reverse relations with model complexity. Therefore, there is a need to find the most important features and then select the optimal feature number. To this end, the effect of each feature on the estimated target was investigated. The importance of a feature is defined as the total number of times that the feature was selected for a leaf node production in the XGB algorithm. Fig. 9 presents the calculated importance of each feature using the Permutation importance method. Based on this method, the evaluation of the model based on all features is calculated to be the base accuracy. Then, each feature will be shuffled randomly one by one, and the model performance is re-evaluated for each case. After comparing the base accuracy with the obtained one, the decrease in the accuracy will be considered and resulted in the importance of each feature.

Table 5
The statistical evaluation metrics of the models with randomly selected hyper-parameters.

Model name	First CV	Second CV	Third CV	Forth CV	Final accuracy
RF (R^2)	0.72	0.85	0.93	0.81	0.83
RF (MSE)	0.0096	0.0106	0.0112	0.0024	0.0085
KNN (R^2)	0.66	0.75	0.91	0.74	0.77
KNN (MSE)	0.0151	0.0415	0.0191	0.0079	0.0209
SVM (R^2)	0.37	0.78	0.94	0.60	0.67
SVM (MSE)	0.0239	0.0390	0.0340	0.0149	0.0280
XGB (R^2)	0.87	0.76	0.92	0.90	0.87
XGB (MSE)	0.0031	0.0039	0.0100	0.0013	0.0046

Table 6
The statistical evaluation metrics of the models with optimized hyper-parameters.

Model name	CV_1	CV_2	CV_3	CV_4	Final accuracy
Optimized RF (R^2)	0.87	0.92	0.85	0.97	0.90
Optimized RF (MSE)	0.0177	0.0305	0.0194	0.0261	0.0234
Optimized KNN (R^2)	0.87	0.93	0.78	0.96	0.88
Optimized KNN (MSE)	0.0468	0.0638	0.0589	0.0302	0.0499
Optimized SVM (R^2)	0.78	0.74	0.57	0.91	0.75
Optimized SVM (MSE)	0.0685	0.1103	0.0833	0.0487	0.0777
Optimized XGB (R^2)	0.88	0.97	0.99	0.95	0.95
Optimized XGB (MSE)	0.0017	0.0036	0.0068	0.0011	0.0033

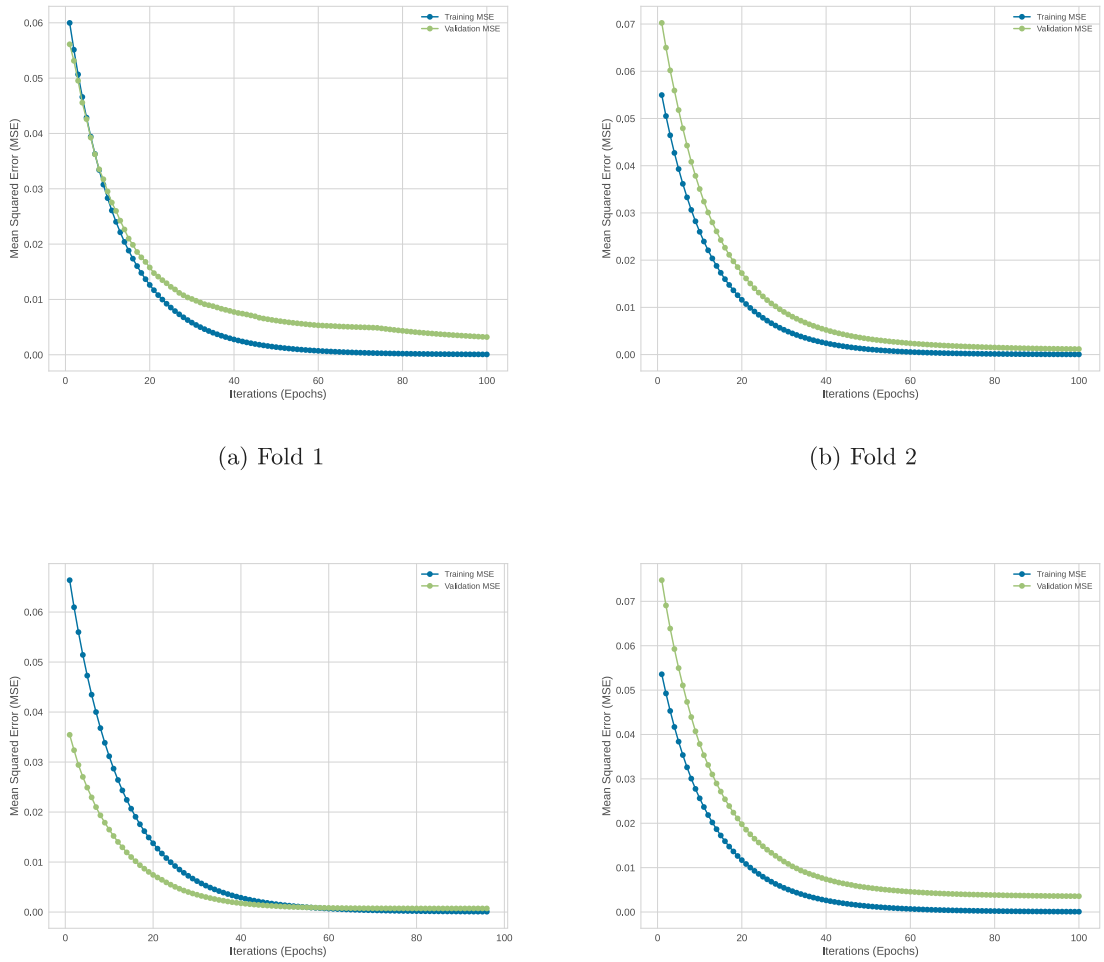

(a) Fold 1 (b) Fold 2

(c) Fold 3 (d) Fold 4

Fig. 7. The loss value (MSE) of train and validation datasets during 100 epochs of training.

The advantages of this method are not to rely on data distribution and the ability to identify the features that cause overfitting. From the importance, the features were subsequently sorted based on their influence on the regression model. Then, the features were added to the selected features' category one at a time, starting with the most important feature.

Since the value of R-squared depends on the number of features in a model [40], another metric termed $\bar{R}$-squared is usually evaluated for comparing models with different numbers of features. Since the number of features differed in each step, the $\bar{R}$-squared of the model constructed from the selected features were considered. The $\bar{R}$-squared was computed as follows:

$$\bar{R}\text{-}squared = 1 - \left[\frac{(1 - R^2)(n\text{-}1)}{(n\text{-}k\text{-}1)}\right] \tag{12}$$

Fig. 10 displays the calculated $\bar{R}$-squared. With the use of $\bar{R}$-squared, the redundant features now have a negative effect on the accuracy. As a result, the optimal number of features with which the model has the highest accuracy could be identified. Fig. 10 indicates that less than three variables resulted in very low accuracy, while more than four features were redundant and unnecessary. As such, four features were identified as the optimal features, including the third quartile of the first IMF's instantaneous frequency (x_3), the center frequency of the first IMF (x_7), the kurtosis of the second IMF's instantaneous frequency (x_{12}), and the center frequency of the second IMF (x_{14}).

The Pearson correlation for all features (Fig. 11) and the variance inflation factor (VIF) for the selected features (Table 7) implies that there is a level of collinearity between variables x7 and x14. This would have been an issue if the purpose of this paper was to interpret the effect of each of those variables on the model performance individually. However, since the primary goal of this paper is to perform prediction, we have not focused on the correlation properties of the features. A similar approach was taken in other studies such as [41].

Moreover, it is known that the XGB as a tree-based ensemble algorithm is robust to the negative effects of the multicollinearity among features as evidenced by findings of [42]. The identified correlated features (x7 and x14) exhibit a level of interaction between one another. This interaction is leveraged by the XGB model to improve the quality of predictions. For example, by adding the feature x7 to the model the adjusted-R^2 has significantly improved from 0.58 to 0.94. This is evident from Fig. 10 where the vertical portion of the plot clearly indicates the significance of the selected variables in improving the regression model's performance.

Fig. 10 shows a recursive feature elimination using the "Yellowbrick" library in Scikit-learn. The graph shows the adjusted-R2 of the model performance across different folds. The solid line represents the mean value of the obtained R2 across different folds using recursively adding the number of most important optimal features. The standard deviation of the model performance is shown as a shadowed line. As such, we can see that the number of four features is selected as the optimal number of features.

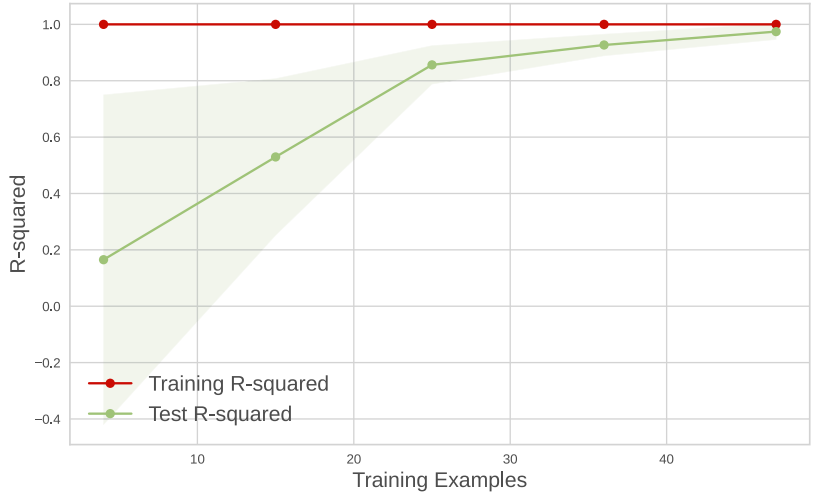

Fig. 8. Learning curve.

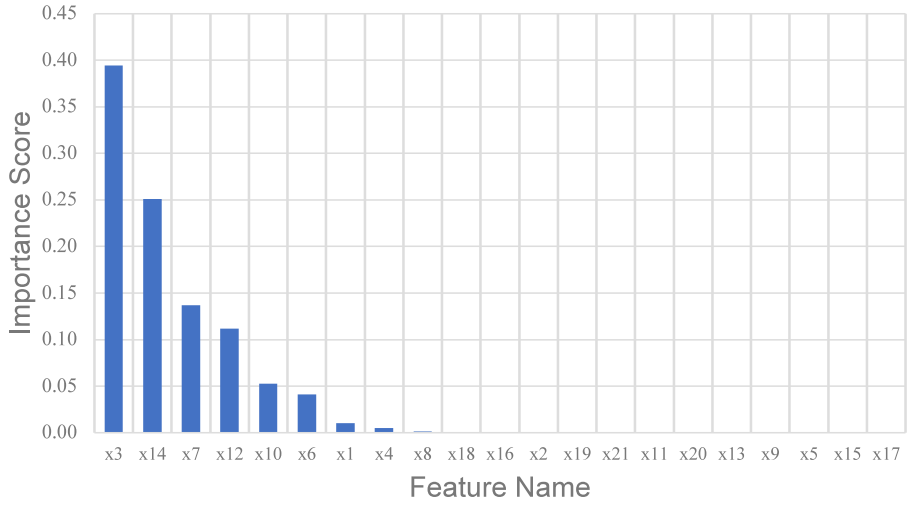

Fig. 9. Feature importance.

Table 7
VIF values of the selected features.

Feature's name	VIF value
x3	2.7
x7	30.3
x12	3.7
x14	27.6

5.2. Discussion on machine learning results

We further summarize the procedures followed thus far. In the first step, the bulk signal was decomposed into an optimal number of IMFs, i.e., three. Then, seven features were extracted from each IMF to build a vector of inputs with twenty-one features. Several machine learning models, namely, RF, KNN, SVM, and XGB were developed, and their accuracies were compared to each other. As a result, XGB yielded the best performance and highest accuracy among all the models. Then, The hyperparameters of the XGB model were tuned, and the model was optimized. In the next step, the tuned XGB was deployed to select the most descriptive features and to find the optimal number of features through multiple iterations. Consequently, four features were introduced, namely, x_3, x_7, x_{14}, and x_{12} (see Table 3).

Figs. 12(a) and 12(b) show the value of x_3 and x_7 versus the bond strength, respectively. The vertical axes show the related bi-surface shear strength. When the bi-surface shear strength is evaluated at more than 3 MPa, both x_3 and x_7 exceed 0.09. This large difference between the features' values is the key to the bond condition clustering. The value of these features can therefore be used to distinguish between quality and poor bond conditions. Figs. 12(c) and 12(d) show the values of x_{12} and x_{14} versus the bond strength, respectively. Since these features are of close values, they are not easily separable. On the other hand, the boundary between the quality and poor bond conditions is more apparent in Fig. 12(d) than in Fig. 12(c), even though they are both extracted from the exact (second) IMF. The reason explained by other researchers [43–45] is that the inhomogeneity increases the chance of the initial wave encountering a scattered wave. This can be explained by nonlinear high-frequency modulations of the ultrasonic wave, interacting with non-linearity and micro-cracks, primarily reflected in the second IMF's statistical features.

Fig. 13 shows the regression error characteristics (REC) curve. The area under the curve (AUC) presents the performance of the regression model. The high value of AUC = 0.855 indicates that the tuned XGB model is highly generalizable [46,47]. The value of the area over the curve (AOC) for the tuned XGB model is calculated as 0.11. This value indicates the adequacy of the model's complexity and the number of selected features. For further details about the background theories of the ROC curves, the readers are referred to [48,49].

Fig. 14(a) shows the range of actual and predicted data. The absolute error for each sample is shown in Fig. 14(b). The error is calculated

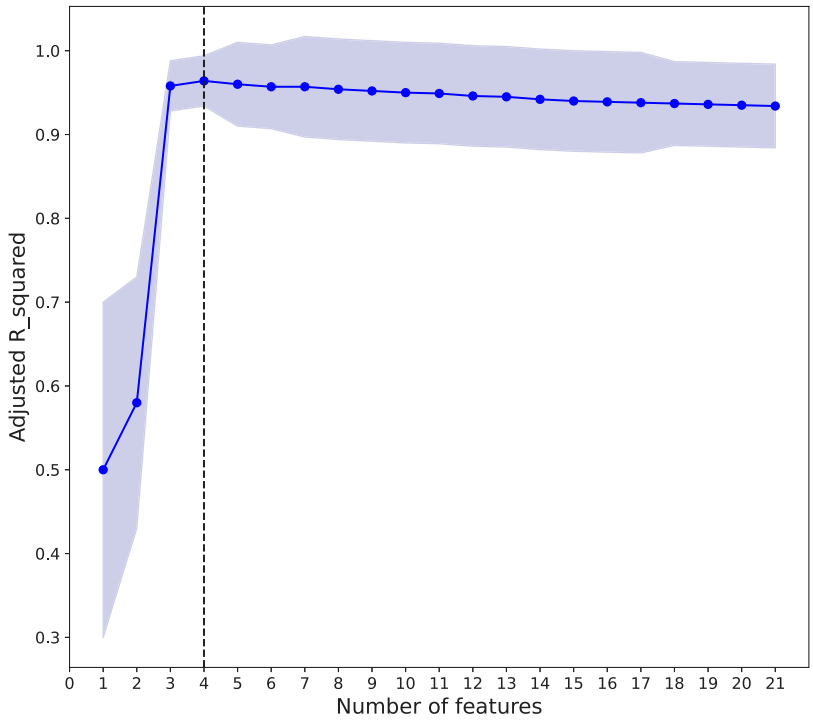

Fig. 10. The recursive feature elimination method to find the optimal number of features.

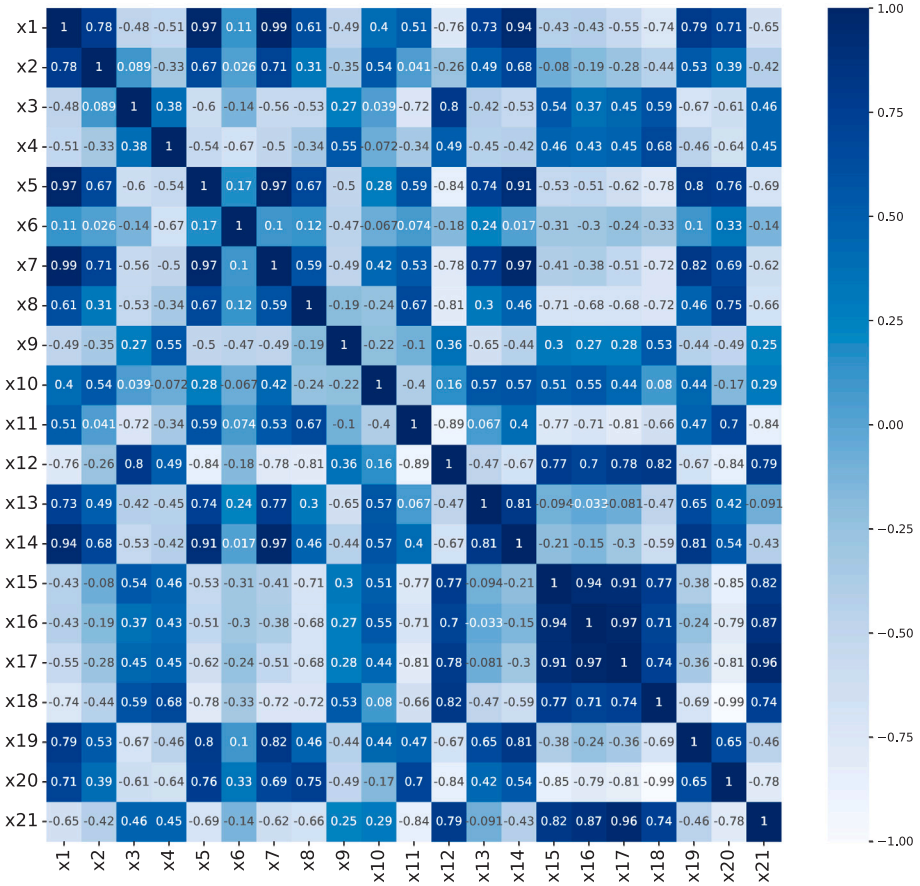

Fig. 11. Pearson correlation coefficients of the features.

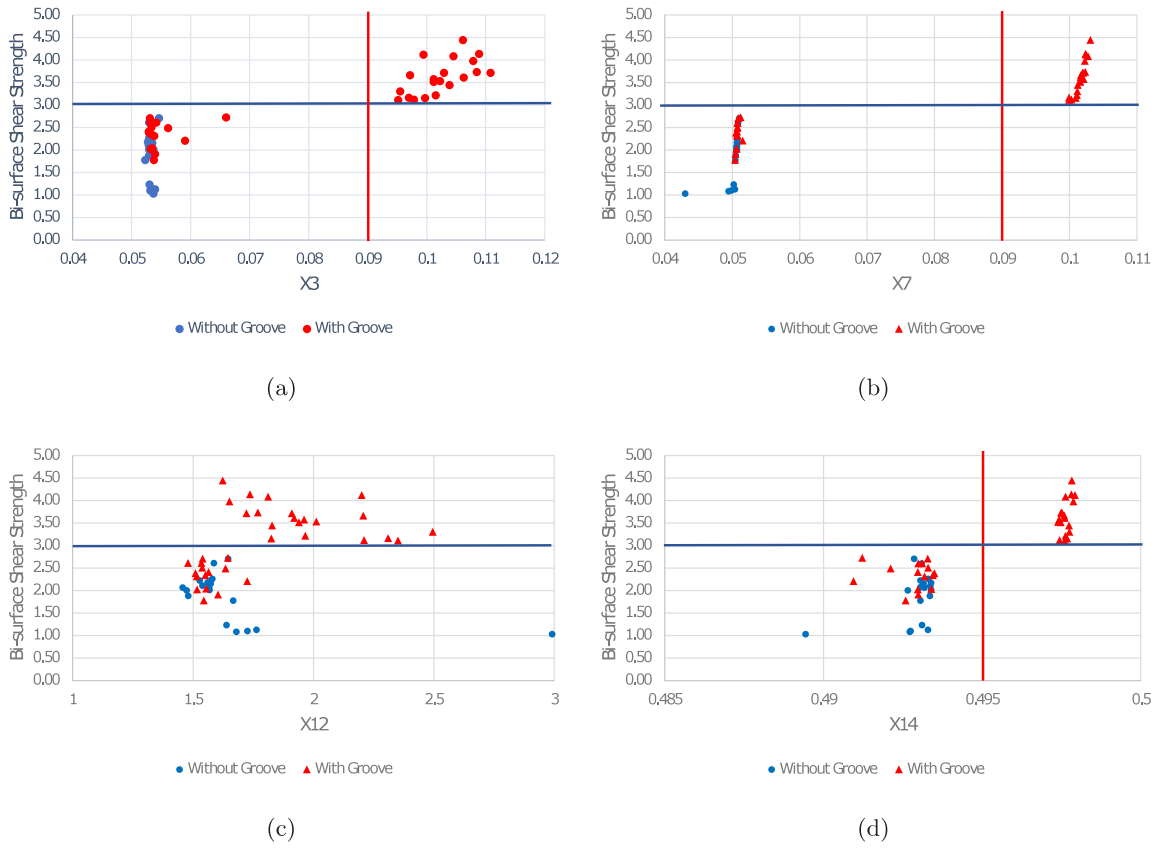

Fig. 12. The selected features values, (a) Third quartile of the first IMF's instantaneous frequency (x_3), (b) Center frequency of the first IMF (x_7), (c) Kurtosis of the second IMF's instantaneous frequency (x_{12}), and (d) Center frequency of the second IMF (x_{14})

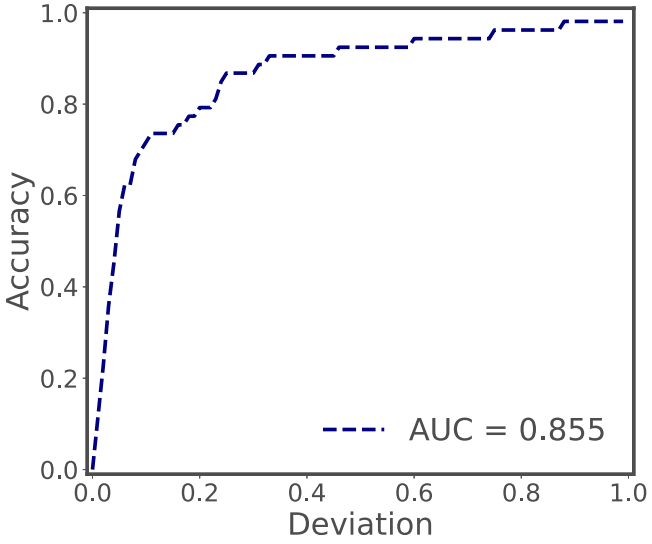

Fig. 13. The regression error characteristic curve.

based on the standardized actual and predicted data. The error means and standard deviation are −0.022 and 0.091, respectively.

A Taylor diagram, depicting the performance of the different machine learning method investigated in this paper, is presented in Fig. 15. The Taylor diagram provides a concise summary of how well patterns match [50]. The presented graph shows the standard deviation of the predicted target resulting from each model and their correlation coefficient, i.e., the regression coefficient. The coefficient of correlation of 1 for the reference point corresponds to the actual data obtained in the experiment. The model with the closest point to the reference point bears the best performance among all the models. Here, the XGB model with the tuned hyperparameters exhibits the best performance.

6. Conclusions

In this paper, a model was proposed for estimating the bond strength of the interfacial transition zone between concrete layers based on ultrasound testing. To test the method, ultrasonic tests and bi-surface shear tests were conducted on layered concrete specimens with different design mixtures and bond zone conditions. It is hypothesized that ultrasonic signals contain information about the concrete material and the bond zone condition from interactions with the material in the form of low- and high-frequency modulation. To retrieve this information, the Variational Mode Decomposition (VMD) algorithm was employed to demodulate the raw ultrasound signal into a pre-specified number of low- and high-frequency sub-signals (IMFs). 21 features were extracted from the optimal number of IMFs, i.e., three. Four different machine-learning algorithms were constructed using the extracted features as input parameters. The accuracies of the models were compared to each other, and the best model with the highest testing accuracy was obtained. The key findings of this study can be summarized as follows:

1. The optimal number of IMFs for signal decomposition is three.
2. There are four optimal features to interpret the characteristics of the modulated signal based on the feature's importance, including the third quartile of the first IMF's instantaneous frequency (x_3), the center frequency of the first IMF (x_7), the center frequency of the second IMF (x_{14}), and the Kurtosis of the second IMF's instantaneous frequency (x_{12}).

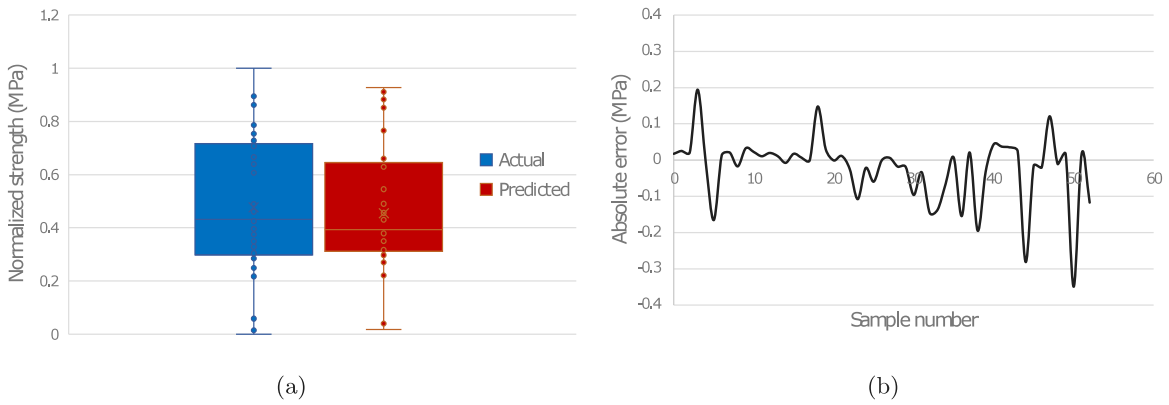

Fig. 14. The range of actual and predicted normalized bond strength and corresponding error.

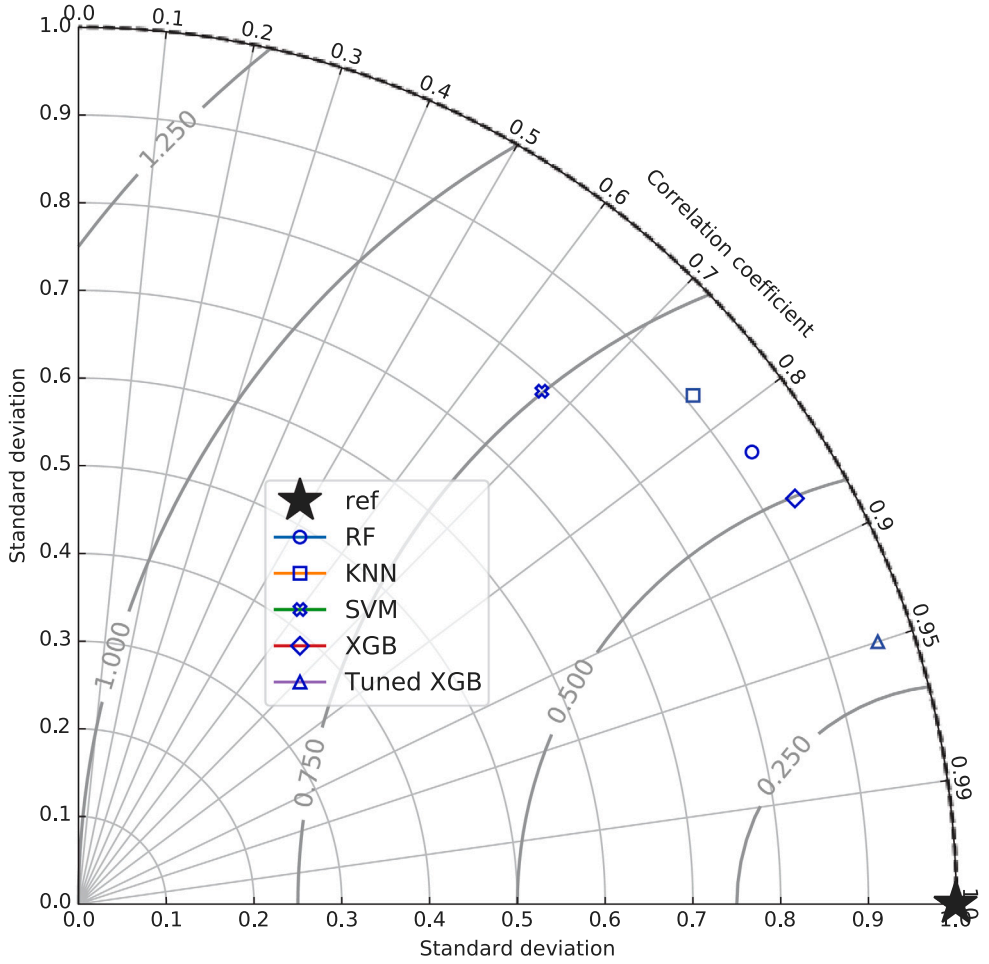

Fig. 15. Taylor diagram representing the performance of the different machine learning models.

3. The optimized XGB bore the highest R^2 accuracy compared to all the other models, i.e., the RF, KNN, SVM, and standard XGB regressor with an R-squared value equal to 95.5 percent.
4. Specimens with the $x_3 > 0.09$, $x_{14} > 0.495$, and $x_7 > 0.1$ had acceptable bond shear strength. Hence, to ensure that the bond zone is in good condition, a feasible space must be constructed based on the boundaries defined by the above-mentioned features.

To optimize the method, the number of 21 independent features proposed in this paper was further reduced to four features to train the optimal model. The identified features are found to be insensitive to the transducer's pressure and couplant amount. Therefore, they can reliably be used for predicting the bond strength of the specimens. These results show the efficiency and robustness of the proposed model in estimating the bond strength condition in bonded concrete based on ultrasonic testing. While this research investigated a wide range of high-performance alkali-activated slag concretes, other research should be conducted on other types of high-performance concretes. In addition, this research used a bi-surface shear test for bond strength evaluation. As such, future work can explore the effectiveness of alternative experimental tests for bond condition evaluation.

CRediT authorship contribution statement

Pooria Khademi: Conceptualization, Methodology, Software, Validation, Formal analysis, Investigation, Resources, Data curation, Writing – original draft, Visualization. **Mohsen Mousavi:** Conceptualization, Methodology, Visualization, Writing – review & editing, Supervision, Project administration, Funding acquisition. **Ulrike Dackermann:** Conceptualization, Visualization, Writing – review & editing, Supervision, Project administration, Funding acquisition. **Amir H. Gandomi:** Conceptualization, Visualization, Writing – review & editing, Supervision, Project administration, Funding acquisition.

Declaration of competing interest

All authors have participated in (a) conception and design, or analysis and interpretation of the data; (b) drafting the article or revising it critically for important intellectual content; and (c) approval of the final version.

This manuscript has not been submitted to, nor is under review at, another journal or other publishing venue.

The authors have no affiliation with any organization with a direct or indirect financial interest in the subject matter discussed in the manuscript.

Data availability

Data will be made available on request.

References

[1] D. Harris, J. Sarkar, T. Ahlborn, Characterization of interface bond of ultra-high-performance concrete bridge deck overlays, Transp. Res. Rec.: J. Transp. Res. Board 2240 (2011) 40–49, http://dx.doi.org/10.3141/2240-07.

[2] L. He, H. Li, W.T. Chow, B. Zeng, Y. Qian, Increasing the interlayer strength of 3D printed concrete with tooth-like interface: An experimental and theoretical investigation, Mater. Des. 223 (2022) 111117.

[3] P. Khademi, V. Toufigh, HPASC–OPCC bi-surface shear strength prediction model using deep learning, Road Mater. Pav. Des. (2022) 1–28.

[4] M. Farzad, M. Shafieifar, A. Azizinamini, Experimental and numerical study on bond strength between conventional concrete and Ultra High-Performance Concrete (UHPC), Eng. Struct. 186 (2019) 297–305, http://dx.doi.org/10.1016/j.engstruct.2019.02.030.

[5] C. Zanotti, N. Randl, Are concrete-concrete bond tests comparable? Cem. Concr. Compos. 99 (2019) 80–88, http://dx.doi.org/10.1016/j.cemconcomp.2019.02.012, URL: https://www.sciencedirect.com/science/article/pii/S0958946518312320.

[6] A. Momayez, M. Ehsani, A. Ramezanianpour, H. Rajaie, Comparison of methods for evaluating bond strength between concrete substrate and repair materials, Cem. Concr. Res. 35 (2005) 748–757, http://dx.doi.org/10.1016/j.cemconres.2004.05.027.

[7] A. Shah, Y. Ribakov, Non-linear ultrasonic evaluation of damaged concrete based on higher order harmonic generation, Mater. Des. 30 (10) (2009) 4095–4102, http://dx.doi.org/10.1016/j.matdes.2009.05.009, URL: https://www.sciencedirect.com/science/article/pii/S0261306909002167.

[8] G. Karaiskos, A. Deraemaeker, D. Aggelis, D. Hemelrijck, Monitoring of concrete structures using the ultrasonic pulse velocity method, Smart Mater. Struct. 24 (2015) http://dx.doi.org/10.1088/0964-1726/24/11/113001.

[9] Monitoring the setting of concrete containing blast-furnace slag by measuring the ultrasonic p-wave velocity, Cem. Concr. Res. 38 (10) (2008) 1169–1176, http://dx.doi.org/10.1016/j.cemconres.2008.04.006.

[10] T. Shiotani, D. Aggelis, Wave propagation in cementitious material containing artificial distributed damage, Mater. Struct. 42 (2009) http://dx.doi.org/10.1617/s11527-008-9388-4.

[11] M. Mousavi, M.S. Taskhiri, D. Holloway, J. Olivier, P. Turner, Feature extraction of wood-hole defects using empirical mode decomposition of ultrasonic signals, NDT E Int. 114 (2020) 102282.

[12] M. Mousavi, A.H. Gandomi, Wood hole-damage detection and classification via contact ultrasonic testing, Constr. Build. Mater. 307 (2021) 124999.

[13] M. Mousavi, A.H. Gandomi, D. Holloway, A. Berry, F. Chen, Machine learning analysis of features extracted from time-frequency domain of ultrasonic testing results for wood material assessment, Constr. Build. Mater. 342 (2022) 127761.

[14] M. Krause, U. Dackermann, J. Li, Elastic wave modes for the assessment of structural timber: ultrasonic echo for building elements and guided waves for pole and pile structures, J. Civ. Struct. Health Monit. 5 (2015) 221–249.

[15] U. Dackermann, B. Skinner, J. Li, Guided wave–based condition assessment of in situ timber utility poles using machine learning algorithms, Struct. Health Monit. 13 (4) (2014) 374–388.

[16] A. Nazerigivi, H.R. Nejati, A. Ghazvinian, A. Najigivi, Effects of SiO2 nanoparticles dispersion on concrete fracture toughness, Constr. Build. Mater. 171 (2018) 672–679.

[17] W. Ren, J. Xu, E. Bai, Strength and ultrasonic characteristics of alkali-activated fly ash-slag geopolymer concrete after exposure to elevated temperatures, J. Mater. Civ. Eng. 28 (2) (2016) 04015124.

[18] W. Ren, J. Xu, H. Su, Dynamic compressive behavior of basalt fiber reinforced concrete after exposure to elevated temperatures, Fire Mater. 40 (5) (2016) 738–755.

[19] N.E. Huang, Z. Shen, S.R. Long, M.C. Wu, H.H. Shih, Q. Zheng, N.-C. Yen, C.C. Tung, H.H. Liu, The empirical mode decomposition and the Hilbert spectrum for nonlinear and non-stationary time series analysis, Proc. R. Soc. Lond. Ser A 454 (1971) (1998) 903–995.

[20] H. Li, Y. Zhang, H. Zheng, Hilbert-Huang transform and marginal spectrum for detection and diagnosis of localized defects in roller bearings, J. Mech. Sci. Technol. 23 (2) (2009) 291–301.

[21] K. Dragomiretskiy, D. Zosso, Variational mode decomposition, IEEE Trans. Signal Process. 62 (3) (2013) 531–544.

[22] S. Mohanty, K.K. Gupta, K.S. Raju, Comparative study between VMD and EMD in bearing fault diagnosis, in: 2014 9th International Conference on Industrial and Information Systems, ICIIS, IEEE, 2014, pp. 1–6.

[23] Y.-J. Xue, J.-X. Cao, D.-X. Wang, H.-K. Du, Y. Yao, Application of the variational-mode decomposition for seismic time-frequency analysis, IEEE J. Sel. Top. Appl. Earth Obs. Remote Sens. 9 (8) (2016) 3821–3831, http://dx.doi.org/10.1109/JSTARS.2016.2529702.

[24] S.L. Kumar, State of the art-intense review on artificial intelligence systems application in process planning and manufacturing, Eng. Appl. Artif. Intell. 65 (2017) 294–329.

[25] L. Ai, V. Soltangharaei, M. Bayat, M. Van Tooren, P. Ziehl, Detection of impact on aircraft composite structure using machine learning techniques, Meas. Sci. Technol. 32 (8) (2021) 084013.

[26] L. Ai, V. Soltangharaei, M. Bayat, B. Greer, P. Ziehl, Source localization on large-scale canisters for used nuclear fuel storage using optimal number of acoustic emission sensors, Nucl. Eng. Des. 375 (2021) 111097.

[27] E. Karbassiyazdi, F. Fattahi, N. Yousefi, A. Tahmassebi, A.A. Taromi, J.Z. Manzari, A.H. Gandomi, A. Altaee, A. Razmjou, XGBoost model as an efficient machine learning approach for PFAS removal: Effects of material characteristics and operation conditions, Environ. Res. 215 (2022) 114286.

[28] H. Zheng, J. Yuan, L. Chen, Short-term load forecasting using EMD-LSTM neural networks with a XGboost algorithm for feature importance evaluation, Energies 10 (8) (2017) URL: https://www.mdpi.com/1996-1073/10/8/1168.

[29] N.-H. Nguyen, J. Abellán-García, S. Lee, E. Garcia-Castano, T.P. Vo, Efficient estimating compressive strength of ultra-high performance concrete using XGBoost model, J. Build. Eng. 52 (2022) 104302.

[30] A. Santamaría, A. Orbe, M. Losañez, M. Skaf, V. Ortega-Lopez, J.J. González, Self-compacting concrete incorporating electric arc-furnace steelmaking slag as aggregate, Mater. Des. 115 (2017) 179–193.

[31] M. Chougan, S.H. Ghaffar, B. Nematollahi, P. Sikora, T. Dorn, D. Stephan, A. Albar, M.J. Al-Kheetan, Effect of natural and calcined halloysite clay minerals as low-cost additives on the performance of 3D-printed alkali-activated materials, Mater. Des. 223 (2022) 111183.

[32] Z. hai Guo, J. Wu, H. yan Lu, J. zhou Wang, A case study on a hybrid wind speed forecasting method using BP neural network, Knowl.-Based Syst. 24 (7) (2011) 1048–1056, URL: https://www.sciencedirect.com/science/article/pii/S0950705111000852.

[33] Y. Zhang, K.-V. Yuen, M. Mousavi, A.H. Gandomi, Timber damage identification using dynamic broad network and ultrasonic signals, Eng. Struct. 263 (2022) 114418.

[34] G.A. Gottwald, S. Reich, Supervised learning from noisy observations: Combining machine-learning techniques with data assimilation, Physica D 423 (2021) 132911.

[35] U.-W. Lok, P. Song, J.D. Trzasko, R. Daigle, E.A. Borisch, C. Huang, P. Gong, S. Tang, W. Ling, S. Chen, Real time SVD-based clutter filtering using randomized singular value decomposition and spatial downsampling for micro-vessel imaging on a verasonics ultrasound system, Ultrasonics 107 (2020) 106163.

[36] F.B. Hildebrand, Advanced Calculus for Engineers, Prentice-Hall, 1949.

[37] D. Zosso, Variational mode decomposition, MATLAB central file exchange, 2020, Retrieved August 27, 2020, URL: https://www.mathworks.com/matlabcentral/fileexchange/44765-variational-mode-decomposition.

[38] H. Yan, Z. He, C. Gao, M. Xie, H. Sheng, H. Chen, Investment estimation of prefabricated concrete buildings based on XGBoost machine learning algorithm, Adv. Eng. Inform. 54 (2022) 101789, http://dx.doi.org/10.1016/j.aei.2022.101789, URL: https://www.sciencedirect.com/science/article/pii/S1474034622002476.

[39] A. Gupta, S. Sharma, S. Goyal, M. Rashid, Novel XGBoost tuned machine learning model for software bug prediction, in: 2020 International Conference on Intelligent Engineering and Management, ICIEM, IEEE, 2020, pp. 376–380.

[40] C. Molnar, Interpretable Machine Learning, Chapter 4: Interpretable Models, Lulu. com, 2020.
[41] M. Mousavi, A.H. Gandomi, M. Abdel Wahab, B. Glisic, Monitoring onsite-temperature prediction error for condition monitoring of civil infrastructures, Struct. Control Health Monit. 29 (12) (2022) e3112.
[42] Y.-H. Deng, X.-Q. Luo, P. Yan, N.-Y. Zhang, Y. Liu, S.-B. Duan, Outcome prediction for acute kidney injury among hospitalized children via extreme gradient boosting algorithm, Sci. Rep. 12 (1) (2022) 8956.
[43] D. Donskoy, A. Zagrai, A. Chudnovsky, E. Golovin, V. Agarwala, Nonlinear vibro-acoustic modulation technique for life prediction of aging aircraft components, in: Proceedings of the 3rd European Workshop - Structural Health Monitoring 2006, 2006, pp. 251–258.
[44] P. Daponte, F. Maceri, R. Olivito, Ultrasonic signal-processing techniques for the measurement of damage growth in structural materials, IEEE Trans. Instrum. Meas. 44 (6) (1995) 1003–1008, http://dx.doi.org/10.1109/19.475146.
[45] S. Selleck, E. Landis, M. Peterson, S. Shah, J. Achenbach, Ultrasonic investigation of concrete with distributed damage, ACI Mater. J. 95 (1998) 27–36.
[46] K. Khosravi, H. Shahabi, B.T. Pham, J. Adamowski, A. Shirzadi, B. Pradhan, J. Dou, H.-B. Ly, G. Gróf, H.L. Ho, et al., A comparative assessment of flood susceptibility modeling using multi-criteria decision-making analysis and machine learning methods, J. Hydrol. 573 (2019) 311–323.
[47] E. Karbassiyazdi, F. Fattahi, N. Yousefi, A. Tahmassebi, A.A. Taromi, J.Z. Manzari, A.H. Gandomi, A. Altaee, A. Razmjou, XGBoost model as an efficient machine learning approach for PFAS removal: Effects of material characteristics and operation conditions, Environ. Res. 215 (2022) 114286, http://dx.doi.org/10.1016/j.envres.2022.114286, URL: https://www.sciencedirect.com/science/article/pii/S0013935122016139.
[48] J. Bi, K.P. Bennett, Regression error characteristic curves, in: Proceedings of the 20th International Conference on Machine Learning, ICML-03, 2003, pp. 43–50.
[49] A. Tahmassebi, A.H. Gandomi, A. Meyer-Baese, A Pareto front based evolutionary model for airfoil self-noise prediction, in: 2018 IEEE Congress on Evolutionary Computation, CEC, IEEE, 2018, pp. 1–8.
[50] K.E. Taylor, Summarizing multiple aspects of model performance in a single diagram, J. Geophys. Res.: Atmos. 106 (D7) (2001) 7183–7192.